TESCAN

TESCAN micro-CT solutions for energy storage materials research

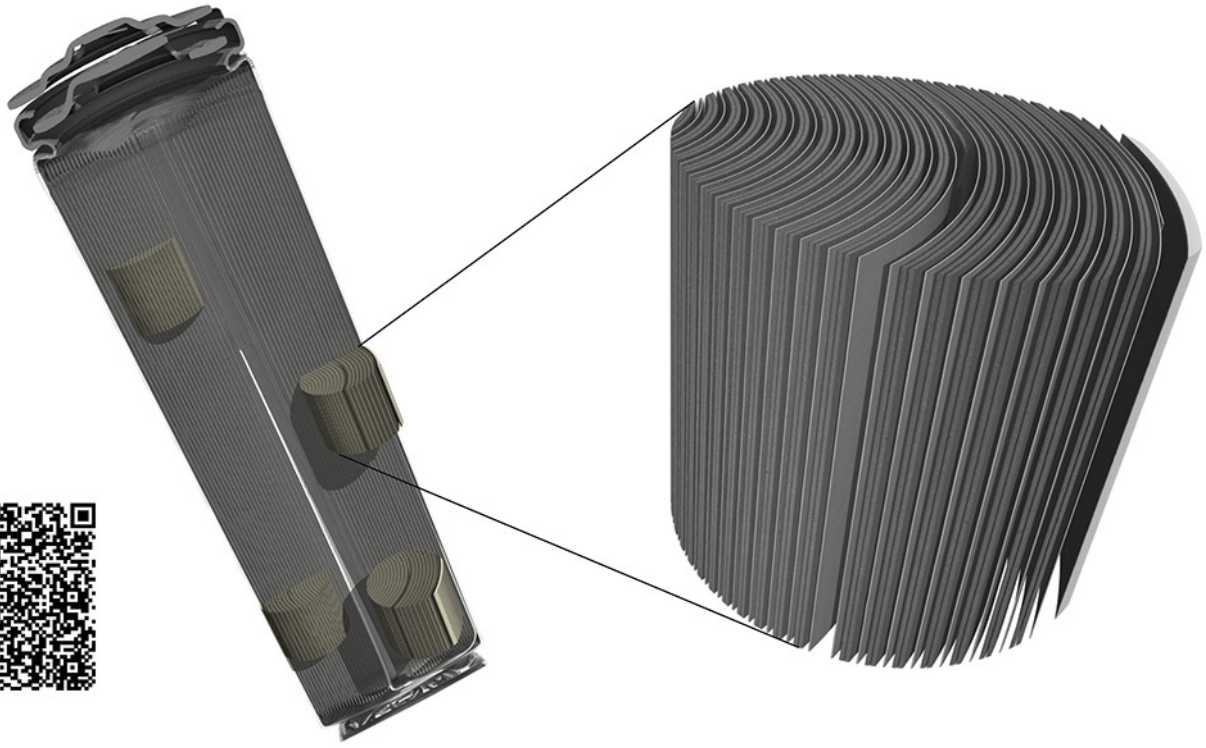

TESCAN UniTOM XL

- ✓ Multi-scale non-destructive 3D imaging optimized to maximize throughput and contrast
- ✓ Fast scanning and high sample throughput with temporal resolutions below 10 seconds
- ✓ Wide array of samples types
- ✓ Enables dynamic tomography and *in-situ* experiments
- ✓ Dynamic screening for synchrotron beamtime
- ✓ Modular and open system with unmatched flexibility for research

Click and find out more

ADVANCED ENERGY MATERIALS
www.advenergymat.de

Nano-Scale Complexions Facilitate Li Dendrite-Free Operation in LATP Solid-State Electrolyte

*Sina Stegmaier, Roland Schierholz, Ivan Povstugar, Juri Barthel, Simon P. Rittmeyer, Shicheng Yu, Simon Wengert, Samare Rostami, Hans Kungl, Karsten Reuter, Rüdiger-A. Eichel, and Christoph Scheurer**

Dendrite formation and growth remains a major obstacle toward high-performance all solid-state batteries using Li metal anodes. The ceramic $Li_{(1+x)}Al_{(x)}Ti_{(2-x)}(PO_4)_3$ (LATP) solid-state electrolyte shows a higher than expected stability against electrochemical decomposition despite a bulk electronic conductivity that exceeds a recently postulated threshold for dendrite-free operation. Here, transmission electron microscopy, atom probe tomography, and first-principles based simulations are combined to establish atomistic structural models of glass-amorphous LATP grain boundaries. These models reveal a nanometer-thin complexion layer that encapsulates the crystalline grains. The distinct composition of this complexion constitutes a sizable electronic impedance. Rather than fulfilling macroscopic bulk measures of ionic and electronic conduction, LATP might thus gain the capability to suppress dendrite nucleation by sufficient local separation of charge carriers at the nanoscale.

1. Introduction

Secondary batteries are a major building block for the intermittent storage of renewable energies as well as a key component in the current e-mobility transition to battery electric vehicles. The state-of-the-art in most devices is based on Li-ion chemistry containing liquid electrolytes. All solid-state batteries (ASSBs), featuring a solid-state electrolyte (SSE), present a potential next-generation technology that promises not only increased operation safety and battery lifetime,[1,2] but also higher performance by enabling the use of Li metal anodes (LMA).[3,4]

Over the last two decades, several classes of highly ion-conductive SSEs have been developed which reach or surpass current liquid-state electrolyte conductivity.[5,6] Yet, no ASSB paying in on the above promises has been developed to date. This is mainly due to mechano-chemical, chemical, and electrochemical stability issues and interfacial processes that have severely compromised any proposed cell's lifetime.[7–11] While many SSE material inherent (mechano-)chemical processing issues seem amenable to modern engineering approaches,[12–19] the situation is less bright regarding the control of interfacial chemical and electrochemical stability (especially when featuring a LMA), as well as ionic and electronic transport quantities across these interfaces. A hitherto missing deep understanding of the structural, chemical, and physical properties of the buried solid–solid interfaces inside ASSBs at the atomic level is required to overcome these performance limiting interfacial issues.

The most studied interfacial properties so far are contact stability and dendrite nucleation and growth.[20–22] Both issues are accentuated for LMA/SSE interfaces. In a first approximation, interfacial stability can be traced back to the

S. Stegmaier, Dr. S. P. Rittmeyer, Dr. S. Rostami, Prof. K. Reuter, Dr. C. Scheurer
Chair of Theoretical Chemistry and Catalysis Research Center
Technical University of Munich
85747 Garching, Germany
E-mail: scheurer@fhi.mpg.de

Dr. R. Schierholz, Dr. S. Yu, Dr. H. Kungl, Prof. R.-A. Eichel
Institute of Energy and Climate Research Fundamental Electrochemistry (IEK-9)
Forschungszentrum Jülich
52425 Jülich, Germany

The ORCID identification number(s) for the author(s) of this article can be found under https://doi.org/10.1002/aenm.202100707.

DOI: 10.1002/aenm.202100707

Dr. I. Povstugar
Central Institute for Engineering
Electronics and Analytics (ZEA-3)
Forschungszentrum Jülich
52428 Jülich, Germany

Dr. J. Barthel
Ernst Ruska-Centre for Microscopy and Spectroscopy with Electrons (ER-C 2)
Forschungszentrum Jülich
52428 Jülich, Germany

S. Wengert, Prof. K. Reuter, Dr. C. Scheurer
Theory Department
Fritz-Haber-Institut der Max-Planck-Gesellschaft
14195 Berlin, Germany

Prof. R.-A. Eichel
Institute of Physical Chemistry
RWTH Aachen University
52074 Aachen, Germany

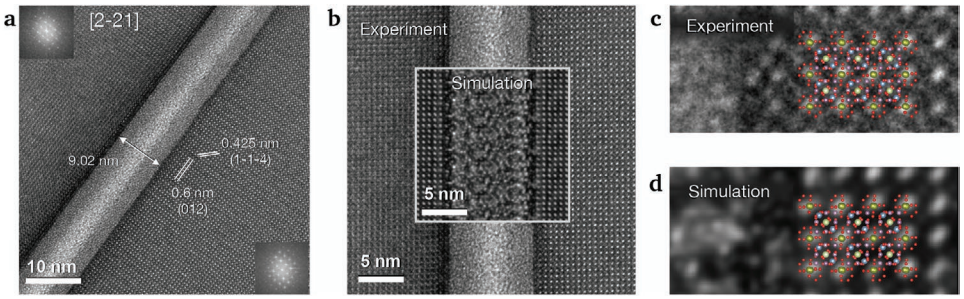

Figure 1. Experimental and simulated TEM images. a) TEM image of LATP crystalline grain with partially wetted amorphous grain boundary. b) Close-up of the grain boundary aligned with a simulated TEM image of the established atomistic model. The pseudocubic arrangement of brighter reflexes both in the c) experimental, and d) simulated TEM image can be attributed to interference at lithium positions. Elemental colors of the overlayed atomistic structure are chosen as Li ●, Al ●, Ti ●, O ●, and P ●.

bulk thermodynamics of the phases in contact. This has been assessed experimentally and through computational materials screening.[19,23] The indicated persistent lack of sufficiently stable bulk SSE materials has led to research into coating materials and the formation of extended interphases akin to the solid electrolyte interphase (SEI) in liquid electrolyte batteries. Yet, finite, nanometer sized interphases which are known to occasionally form between ceramic grains[24] can potentially also stabilize the interface. These interphases have recently been termed complexions for the case when they are thermodynamically self-limiting in thickness and may exhibit distinctively different stoichiometries, structure, and properties than either of the neighboring bulk phases.[24–27]

Dendrite nucleation has been discussed as closely related to local electrochemical stability. Within the SSE, the necessary reduction of a Li^+ ion to metallic Li to form a dendrite nucleation site will only proceed if no more easily reducible center, most likely a transition metal (TM) ion,[28,29] such as Ti^{4+}, is available in the vicinity and reachable by the electron, for example, by polaron hopping.[30,31] Penetration of the mechanically softer grain boundary network within the SSE plays a crucial role in dendrite nucleation and subsequent growth.[20,32] One way to stop dendrite growth within the SSE could correspondingly be the embedding of reducible particles as electron traps. Reducing the number of available electrons would be a complementary way to suppress dendrite formation and enhance SSE stability. To this end, Han et al. recently put forward a bulk estimate that a dendrite-free operation at current densities of ≈1–10 mA cm^{-2} necessitates SSE electronic conductivities below ≈10^{-10}–10^{-12} S cm^{-1}.[33]

No SSE material simultaneously meeting both requirements of a satisfactorily large ionic conductivity and such an extremely low electronic conductivity has been reported so far. Intriguingly, however, the natrium super ionic conductor-type (NASICON) SSE material $Li_{(1+x)}Al_{(x)}Ti_{(2-x)}(PO_4)_3$ (LATP) has a confirmed high ionic mobility (reaching a maximum at an Al^{3+} content of $0.3 \leqslant x \leqslant 0.4$),[34–36] and a high stability against dendrite formation and dendrite growth over long cycling times was reported.[37,38] At the same time, DC polarization measurements (see Section S1, Supporting Information) yield a bulk electronic conductivity of $4.7 \cdot 10^{-9}$ S cm^{-1} at 50 °C, which is by 1–3 orders of magnitude larger than the suggested critical value by Han et al.[33] Motivated by this puzzle, we recognize that local electrochemical stability and charge carrier mobility (i.e., of ions and electrons) can vary vastly over dimensions of only a few nanometers. This is actively exploited in semiconductor physics[39] and nano-ionics.[40,41] We correspondingly hypothesize that a nanometer-scale complexion interphase forms at the boundary of LATP grains and it is this interphase and its particular properties that can be exploited toward high stability and dendrite suppression capability of this SSE.

Aiming to confirm this hypothesis with an atomic level picture we combine high-resolution electron microscopy, atom probe tomography, and first-principles based simulation to establish a defined structural model of the LATP grain boundary interface. Simulations based on first-principles density-functional theory (DFT) have contributed greatly to the progress in energy material discovery and design by accelerating materials screening and by linking diverse experimental data to provide detailed mechanistic insight into their function.[23,42,43] While most studies aim at a deeper understanding of the bulk behavior especially for crystalline phases of battery materials,[44,45] only recently focus has been drawn also on the bulk of amorphous ceramic SSE materials.[46,47] Here, we show how a closely interlinked experiment-theory approach allows to close the complexity gap to interfaces involving the formation of an amorphous interphase capped by a distinct complexion at the surface of the crystalline grains. For the LATP grain boundary, we indeed find the formation of such an interphase complexion, which exhibits high Li ion mobility in its amorphous part, but a high electronic impedance across its thin region with residual order. Rather than meeting Han et al.'s bulk criterion of an excessively low electronic conductivity, the LATP stability thus seems to derive from a local spatial separation of charge carriers at the nanoscale. Broadly speaking the grains are coated by a spontaneously forming complexion that prevents mobile Li ions from meeting reducing electrons, a concept once actively engineered could be a promising route to handle dendrite formation and make ASSBs a technological reality.

2. Results and Discussion

2.1. Transmission Electron Microscopy

(Scanning) Transmission electron microscopy ((S)TEM) measurements were carefully conducted for a prototypical LATP grain boundary to minimize electron beam induced changes as

much as possible. The high resolution (HR) TEM image shown in **Figure 1**a clearly shows a pronounced intensity profile across the grain boundary domain of ≈9 nm width. From this contrast three regions can be differentiated: the crystalline LATP grains, thin and darker semi-amorphous regions to both sides at the crystalline grain interface, and a brighter amorphous region in the grain boundary center. Both grains are oriented in $[2\text{-}21]_{hex}$ zone axis. The highly symmetric bright reflexes in Figure 1c correspond to a $[100]_{pc}$ pseudocubic sublattice commonly assigned to partially occupied Li positions in the LATP crystal structure. It is important to note though that this pattern is formed due to constructive interference of electron waves scattered off neighboring transition metal centers and does not arise directly from scattering off the highly mobile Li ions with small scattering factor. The grain terminating planes of the crystalline region are indexed as $(012)_{hex}$-planes and most likely formed by Li-O planes or Al/Ti-P-O planes. Due to residual beam damage, the exact assignment of the terminating planes could not be resolved unambiguously in the high-angle annular dark field (HAADF) HR-STEM experiment (Figure S3, Supporting Information) and will be addressed by simulations below. The significantly brighter signal of the central part of the amorphous region between the crystalline LATP grains might at first simply be rationalized in terms of the lower relative density of the amorphous phase (94% of the LATP crystalline density),[48] possibly superimposed by a reduced sample thickness for example due to preferential milling during sample preparation. A dark contrast in HAADF-HRSTEM (see Figure S3, Supporting Information) with concomitant reduced total energy dispersive X-ray spectroscopy (EDS)-counts might also point to a thickness effect. For amorphous Li_3PO_4 and $AlPO_4$ in triple points between grains (see below) similar effects have been observed before.[49,50] In order to scrutinize this interpretation we performed explicit TEM simulations[51] based on fully relaxed atomistic models (see below). As detailed in Section S4.3, Supporting Information, these simulations are specifically tested for the effect of reduced thickness and local density, but neither can quantitatively reproduce the observed intensity gradient over the amorphous region. We therefore hypothesize that the latter results at least partially for example, from a non-uniform grain boundary narrowing along the beam direction or inelastic scattering effects like interband transitions that are currently not accounted for in the TEM simulations.

TEM analyses of multiple such LATP grain boundaries yield widths in the range of 5–20 nm, which is in agreement with data reported from atomic force microscopy line scans.[52] The variable width amorphous region of these grain boundaries, cf. Figure 1a, might at first be interpreted as incipient wetting by a secondary phase. In a previous SEM and STEM EDS study two secondary phases were detected in triple points of the same material.[49,50] They were identified as $AlPO_4$ and presumably Li_3PO_4, suggesting these as possible stoichiometries also for the amorphous grain boundary region. The formation of these two secondary phases due to microstructural effects of densification in ceramic LTP upon the insertion of Al^{3+} has been discussed earlier.[34,35,48] While especially $AlPO_4$ is known to have a beneficial influence on the mechanical binding of grains in LATP polycrystalline material upon thermal treatment, the Li ion conductivity of both secondary phases is low. Their formation would, hence, impede ion diffusion pathways [48,53,54] and decrease the material's overall conductivity significantly. For the grain boundaries analyzed here, STEM-EDS (Figures S3–S5, Supporting Information), as well as atom probe tomography (APT) experiments described further below, cf. **Figure 2**c, show only slight variations of Al and Ti content, though. This rules out both of the known secondary phases as candidates for the here observed LATP grain boundary interphase. Being interested in its intrinsic properties, we thus focus on a grain boundary which is not wetted by a secondary phase in the following.

2.2. Atom Probe Tomography Analysis

As Li-mapping by STEM-EDS is not possible and STEM electron energy loss spectroscopy measurements suffered from

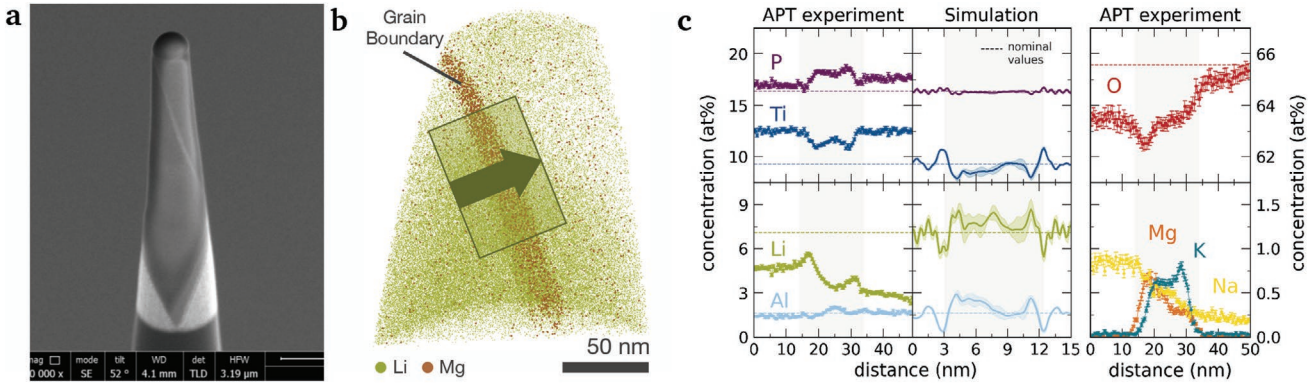

Figure 2. Atom probe tomography measurements. a) Pt deposited APT needle with LATP specimen featuring a grain boundary. b) Reconstructed atom map clearly showing the grain boundary by exploiting the high contrast of accumulated Mg impurities. c) Corresponding atom profiles for each element across the grain boundary (the overlayed rectangle in panel (b) indicates the selected subvolume used for averaging, with the arrow indicating the direction used for positive distances) from APT experiment and related elemental profiles from simulation, cf. Section S4.3, Supporting Information. Simulated profiles are noisier due to the smaller volume available for averaging and a shift to the nominal crystalline stoichiometry (dashed lines) has been applied for the major species (for details see Section 2.3.1) to allow for a comparison with experimental ionic conductivities which are taken from a statistical ensemble of multiple LATP grains.

severe beam damage, we complemented the TEM investigations by APT analysis. APT is able to reveal the 3D elemental distribution at the nanoscale level, including the one for Li. The APT results shown herein suggest a change in chemical composition from nominal stoichiometric LATP at the grain boundary. With these frontier measurements, we extend the APT application field from predominant metallurgy, semiconductor research and only recently battery cathode materials, such as lithium-manganese oxides,[55–59] to Li ion conducting solid state electrolytes.

An SEM image of an APT needle-shaped specimen prepared from LATP is shown in Figure 2a. Due to brighter contrast, the grain boundary presence can be distinguished at the specimen surface in SEM, cf. Figure 2a. For reasons of visualization the high contrast of residual Mg^{2+} accumulated in the grain boundary is exploited to localize the grain boundary position in the 3D APT atom map shown in Figure 2b. A detailed description of the sample preparation procedure, APT measurement conditions as well as data reconstruction and analysis is given in Section S3, Supporting Information. The resulting detailed and spatially-resolved experimental elemental concentration profiles across the grain boundary are presented in Figure 2c. They disclose bulk concentrations of Ti, Al, and P close to the nominal LATP stoichiometry (dashed lines). At the grain boundary, Ti is locally depleted by about 1.5 at% at the expense of predominantly P. The further observed underestimation of the oxygen content by a few at% is a known APT artifact which can be attributed to the field evaporation of neutral species or post-dissociation of oxygen-containing complex ions,[56,58,59] such as P_xO_y and TiO_x (see Figure S6, Supporting Information). The exact oxygen distribution in the atomistic models established below will thus not be linked directly to the APT data but derived from structural TEM data in conjunction with force field based simulation.

The most striking information retrieved from APT is the Li distribution. The substantial asymmetry between the grains to the left and right of the boundary indicates a notable inhomogeneity of the synthesized material at the microstructural level. Even more important is the notable Li-enrichment at both sides of the grain boundary strip, which aligns well with the observed Ti-depletion across the grain boundary. We note that the absolute Li concentration delivered by APT may be biased due to its low evaporation field[59] as well as possible Li mobility under high electric fields. This requires further investigation for the future use of APT on SSEs. Nevertheless, the information on the relative Li distribution across the grain boundary remains reliable, since the grain boundary plane is virtually normal to the specimen surface at the moment of the field evaporation, and hence parallel to electric field lines determining the possible Li in-run migration pathway.

In addition to the primary LATP elements, cationic impurities of Na^+, Mg^{2+}, and K^+ are also detected by APT with low local concentrations never exceeding 1 at%, cf. Figure 2c. Na contamination probably originates from the sample polishing prior to the preparation of TEM and APT specimens. This assumption aligns with the observed predominant Na^+ localization in the top (closest to the original surface) region of the APT dataset. Mg and K, which may have been introduced during LATP synthesis, accumulate in the grain boundary streak. Yet, with local concentrations below 1 at%, the absolute number of ions in the LATP electrolyte lies within the 30–150 ppm regime, assuming a brick-layer model with experimental grain edge length and grain boundary widths.[52] The effect of cationic impurities on electrolyte properties is very specific to the impurity itself and cannot be generalized. While the integration of Na^+ ions into the LATP framework is not surprising for a sodium-type ion conductor (NASICON), Na^+ ions are not expected to show high mobility through Li-ionic channels due to a larger ionic radius.[60] The same holds for the monovalent K^+ which, due to its even larger radius,[60] is not incorporated into crystalline sites but rather accumulates in the grain boundary. In contrast, the introduction of divalent cations such as Mg^{2+} with similar ionic radii as Li^+ may have a beneficial effect on Li ion mobility by the introduction of additional vacancies. Similar enhancement of charge carrier diffusivity in SSEs by doping with higher-valent cations has been of interest also in recent multivalent-ion battery studies and selective interfacial doping might provide an additional design degree of freedom for future interface engineering.[61–64] However, the small amount of Mg^{2+} impurities found herein is not expected to affect the energetic or structural properties of the LATP host targeted in this work, as well as the possible influence of the observed amorphous interphase formation on conductivity.

2.3. Molecular Dynamics Structural Models and TEM Simulations

We therefore proceed with molecular mechanical simulations employing a first-principles derived force field specifically parameterized to reproduce the key structural and dynamic properties of LATP. The parameterization scheme as well as force field validation through DFT calculations is detailed in Section S4.1, Supporting Information. With this force field we establish atomistic structural models of the complex grain boundaries and subsequently use them as the basis for dynamical simulations of ionic diffusion. While structurally simple grain boundaries have been studied extensively by simulations,[65] they are mostly modeled as clean, infinitely sharp interfaces between two tilted grains that is constructed from coincidence lattices.[32,66–68] Only recently Kim et al. have introduced a first approach to model glass–ceramic interfaces by fusing together two structurally different phases.[47] However, none of these setups would be suitable for the complex, multi-phase interfacial structure of the LATP grain boundary as evidenced by the TEM and APT data. In order to properly capture a possible formation of finite-width surface complexions at the grain surface and the gradual transition into an amorphous, glassy interphase we therefore develop a computational sintering protocol that explicitly draws on the experimental information from our TEM and APT measurements. A detailed account of this protocol is provided in Section S4.2, Supporting Information, and we here provide only a concise description of its cornerstones. The proposed sintering protocol itself is fairly universal, and thus in principle applicable to other ceramic SSE grain–grain interphases. However, the exact simulation parameter values which are retrieved from a design of experiment approach need to be reevaluated for each individual case.

2.3.1. Atomistic Modeling and TEM Simulations

Similar to Kim et al.,[47] the starting point is a two-slab model, comprising a crystalline and a glass-amorphous phase. For the crystalline grain a supercell is constructed from the LATP ICSD structure (ID: 253240).[69] The grain orientation and surface cut is chosen according to the TEM findings in $[2\text{-}21]_{hex}$ direction. Analysis of differently terminated and structurally relaxed grain surface models against vacuum indicates a clear energetic preference for an Al-rich surface termination (see Figure S12b). A corresponding Ti depletion at the grain surface is consistent with the APT elemental profiles across the grain boundary shown in Figure 2c above. The amorphous domain of the two-slab model is subsequently built from stochastically sampled LATP building blocks and following the relative chemical composition extracted from the APT measurements. Phosphate ions are treated as fixed units, somewhat limiting the flexibility for an exact match with the APT phosphorous profile for example, due to the systematic absence of conceivable polyphosphate units, and local charge neutrality is assumed to compensate for the afore discussed lack of information on the exact oxygen distribution from the APT data. The experimentally observed profiles have moreover been shifted to fit nominal elemental values for the crystalline grain domain. This shift is necessitated by the later analyses in which Li ionic conductivities from simulations are compared to experimental values, which are obtained from LATP pellets comprised of numerous grains. Rather than reconstructing the exact composition of one LATP grain realization from experimental APT profiles we have opted for constructing an interface model which is representative for the ensemble composition. The resulting profiles obtained for the simulation models are shown in Figure 2c. A more detailed description of the adjustments performed on the experimental composition and a discussion of deviations therefrom is given in Sections S4.2 and S4.3, Supporting Information. The resulting two-slab model is then subjected to a computational sintering, consisting of an initial densification by uniaxial pressing and heating, followed by a melting, and final quenching steps both realized by molecular dynamics (MD) simulations. The detailed parameters (target density, melt temperature, and equilibration times) are determined from a fullfactorial design of experiments analysis to maximize the energy lowering induced by the sintering and to lead to a final structural model with an average mass density in the grain boundary area matching the experimental estimate. Averages over a total of five such grain boundary models are finally taken to account for the stochastic nature of the amorphous interphase. As detailed in Section S4.3, Supporting Information, the resulting models exhibit (partially by construction) structural and compositional characteristics that fully match the TEM images and APT elemental profiles within the uncertainties of the employed force field and the choices to be made to accommodate the restrictions imposed by limited statistics in experiment and simulation. Figures 1b–d illustrate this with a simulated HR-TEM image that reproduces both crystalline and amorphous regions of the extended grain boundary. A full analysis of TEM contrast comparison of experiment and simulation is provided in Section S4.3, Supporting Information.

As a most striking independent outcome that was not seeded by construction, the structural models exhibit a distinct thin region at both sides of the grain boundary strip exactly as observed by TEM. As illustrated in the three middle cuts displayed in the lower row of **Figure 3**a, this region is characterized by a gradual loss of structure from the crystalline grain to the fully amorphous interphase in the center of the boundary. We perform a quantitative analysis of the width of this intermediate region by means of 2D Fourier transforms of the Ti-Al framework as described in Section S4.4, Supporting Information. In particular this is done for simulation cells of varying width, in which the initial amorphous part after application of the sintering protocol takes between 40% and 48% of the total width. Intriguingly and as shown in Figure 3b, within error bars the width of this intermediate region is found to be constant, identifying the region as a complexion with a thermodynamically self-limited width. Chemically, the most notable feature of the complexion is a complete Ti depletion at the edge of the crystalline grain as, to a lesser degree, also indicated by the APT elemental profiles. The preference for an Al-rich surface termination already seen against vacuum thus prevails also within the grain boundary complexion. To scrutinize this important insight we deliberately swapped surface Al ions with Ti subsurface ions in the atomistic models. Such artificially created Ti-terminated models consistently show higher free energies than the true model, cf. Figure S22, Supporting Information, confirming that the Ti depletion is not an artefact of the initial setup of the two-slab model.

2.3.2. Li Diffusion Simulations and Ion Conductivity

The established structural models allow to perform extensive MD simulations at varying temperatures and analyze the Li ion diffusion in the different domains of the grain boundary. We use the Nernst–Einstein relation to convert the obtained atomistic mean-square displacements to macroscopic conductivities as described in Section S4.5, Supporting Information. Figure 3c displays these conductivities, separately for the crystalline grain, the amorphous interphase and the complexion in between. The crystalline conductivity exhibits generally good agreement with bulk experimental values reported by Mertens et al.,[52] especially in the extrapolated elevated temperature regime. At ambient temperatures a direct comparison to experiment must be handled with care since the simulated macroscopic conductivities are somewhat encumbered by larger statistical errors. A comprehensive evaluation of the error estimates is given in Section S4.5, Supporting Information. Mechanistically, the simulations fully confirm previous experimental reports[70] that attribute this high conductivity to the presence of Li-ion channels in the crystalline LATP structure, cf. Figure S26, Supporting Information. In this respect, the comparably high conductivity inside the amorphous phase is at first sight surprising, but then readily rationalized by the lower atom density of this region.[48] The somewhat higher ion impedance within the complexion is correspondingly likely caused by a mechanistic change from well-defined ion migration pathways with shallow free energy barriers in the crystalline grains to free volume dominated hopping in the amorphous interphase. In

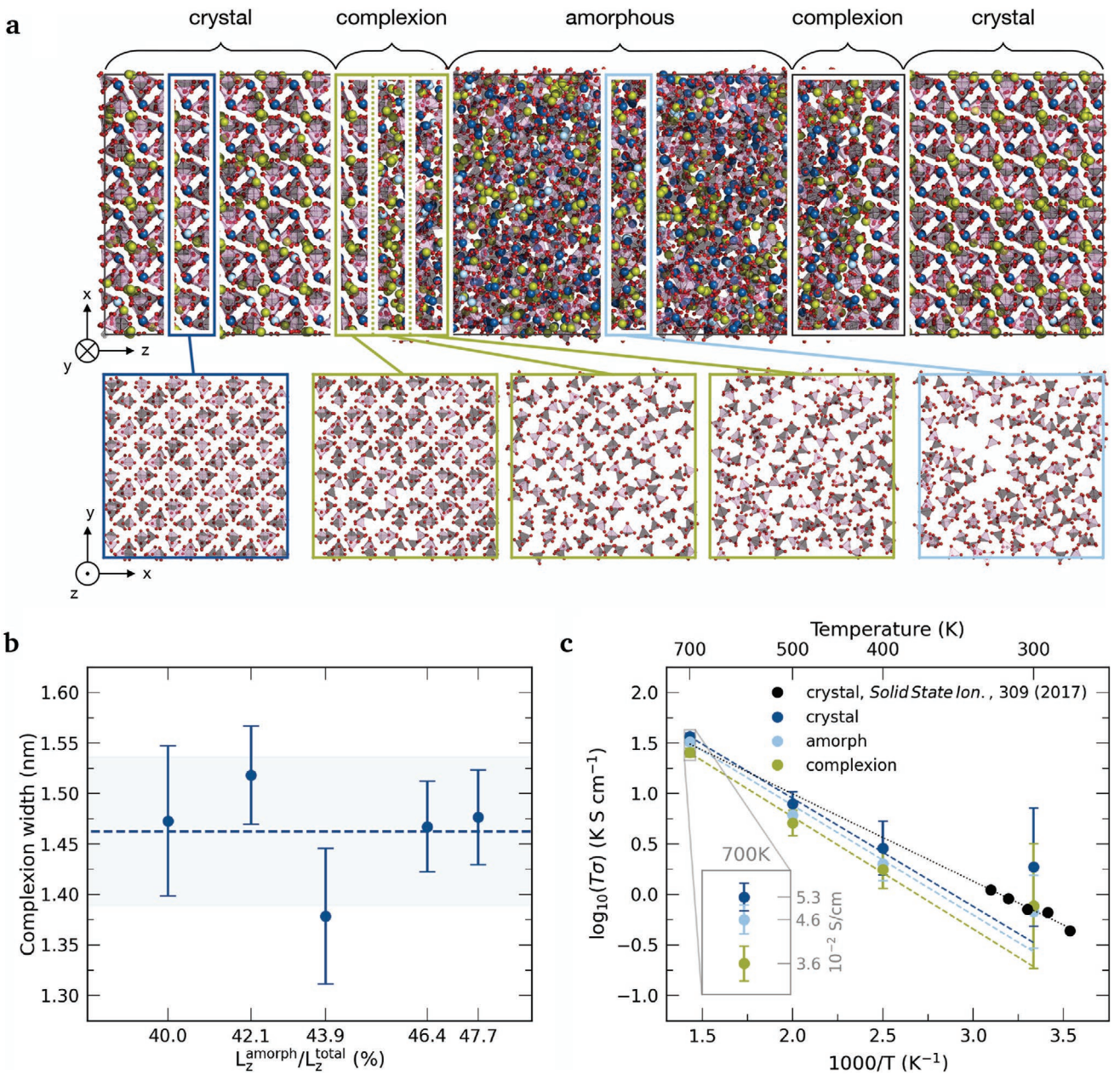

Figure 3. Atomistic grain boundary model and dynamical simulations. a) Atomistic model of the grain boundary domain, showing the crystalline grains, the amorphous interphase and the semi-amorphous complexions at the grain surfaces. Elemental colors are chosen as Li ●, Al ●, Ti ●, O ●, and P ●. The gradual loss of structure across the grain boundary is illustrated by five close-ups displaying LATP phosphate units. b) Width of the complexion as quantified by 2D Fourier transforms for simulation cells in which the fraction of the amorphous part (L_z^{amorph}/L_z^{total}) after computational sintering varied between 40% and 48% of the total simulation cell width L_z^{total}. c) Arrhenius plot with the domain-resolved Li ion conductivities as determined from MD simulations. Also shown are experimental values from Mertens et al. for crystalline LATP bulk.[52] Calculation of error bars in panels (b) and (c) is described in Section S4.5, Supporting Information.

addition to the geometrical obstruction of Li ion mobility by the narrowing and ebbing of ion channels within the complexion, cf. Figure S27, Supporting Information, the local Ti-depletion in the complexions is expected to lower the diffusivity even further, in that the reported aluminum content between $0.3 \leqslant x \leqslant 0.4$ for optimal Li conductivity in LATP is formally exceeded, thus possibly affecting the mobile charge carrier density.[34–36] A recent study by Pfalzgraf et al. tackles exactly these two effects of chemical and geometrical changes in LATP on the Li migration.[71]

By a model decomposition of macroscopic electrochemical impedance spectroscopy (EIS) data into bulk and interface contributions, Mertens et al. had concluded on an orders of magnitude lower interfacial conductivity.[52] The present MD data suggests this lower conductivity to rather arise from limited contact areas or residual secondary phases of extremely

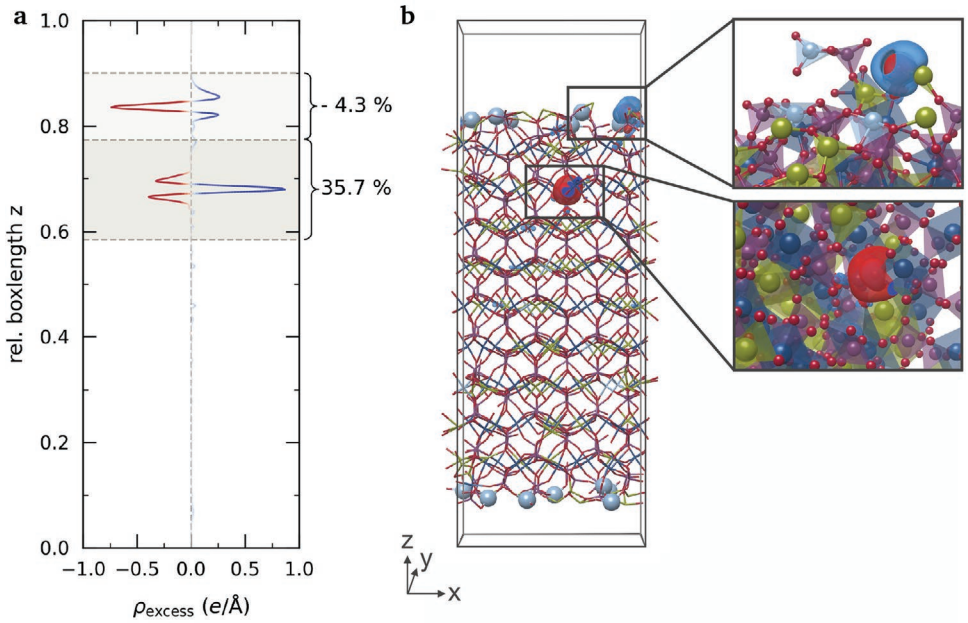

Figure 4. DFT calculations of localized electronic excess charge in the Ti-depleted complexion. a) Electronic excess charge density ρ_{excess} over the simulation box length and averaged over planes parallel to the surface. Positive (negative) values indicate electron accumulation (depletion). The excess electron is mainly located in sub-surface layers containing Ti^{4+} ions, as demonstrated by the integral of the excess density (dark gray shaded region). A delocalization of excess electron density (≈52 %) among bulk Ti^{4+} ions is a known artifact in semi-local functionals such as generalized gradient approximation (GGA)[30,73] and is discussed in Section S5, Supporting Information. The rearrangement of electronic density even withdraws a small amount (–4.3%) of electron density from the surface layer. b) Corresponding side view of the simulation box with superimposed isosurfaces of electron depletion (red, –0.805 e Å^{-3}) and electron accumulation (blue, +0.916 e Å^{-3}), confirming the Ti^{4+} ions as location of a generated small polaron.

low Li ion conductivity[49,50] than be an intrinsic feature of LATP grain boundaries. As an intriguing corollary, the observed high capability of LATP to suppress dendrite nucleation within the SSE and penetration into the grain boundary network can thus not result from a lack of Li ion mobility in the grain boundaries.

2.4. Electronic Structure Calculations

As the latter results suggest an electronic reason behind the dendrite suppression we proceed to DFT calculations and analyze the localization of excess electrons at the grain boundary (see Section S5, Supporting Information, for computational details). With a previously measured lower electronic conductivity ascribed to the reduced structural order of the grain boundary domain,[72] we specifically focus here on the identified complexion and its distinctly different chemical composition. As this Ti-depletion at the edge of the crystalline grain was equally found in the full structural models of the grain boundary and against vacuum, we concentrate the demanding calculations on the latter and compute the excess electron density after injection of one electron for a corresponding Al-rich surface termination.

As shown in **Figure 4** and fully consistent with experimental reports of a favored reduction of Ti^{4+} and Ge^{4+} during cycling of LATP and LAGP, respectively,[28] we find the excess electron to be localized in close proximity to a Ti^{4+} ion. In the Ti-depleted termination, the generated small polaron is thus located in a sub-surface layer, with important consequences for polaron hopping as the main electron conduction mechanism in this ceramic insulator.[30,31,74] Exhibiting an exponential dependence on the height and width of the hopping barrier, this mechanism is highly sensitive to nearest-neighbor (NN) Ti–Ti distances. While this distance is 4.88 Å in the crystalline LATP bulk, the mean shortest Ti–Ti distance as obtained from integrating over the first peak of the Ti–Ti radial distribution function of our full structural grain boundary models is 5.41 Å across the complexion. The Ti depletion in the complexion thus leads to a substantial increase of the Ti–Ti NN distance by more than 0.5 Å between ions in the crystalline grain and in the amorphous interphase. In terms of the electronic conductivity by polaron hopping, such an increase incurs a dramatic anisotropic electronic impedance. Effectively, the complexion acts like an electronically insulating coating around the grain.

3. Conclusions

We have combined structural information from HR-TEM images and complementary high-resolution APT compositional data for cross sections across a grain boundary interface in LATP with a synthesis-inspired MD based theoretical sintering protocol to arrive at realistic, atomistically defined structural models for the multi-layered grain boundary in this SSE material. As most striking feature, we find the formation of a nanometer-thin surface complexion between the crystalline grain and a glass-amorphous interphase of several nanometers width. This

complexion exhibits residual yet slightly amorphized structure visible as a darkened stripe in the TEM images and has a distinct composition, noticeably different from either the crystalline or the amorphous interphase region.[24,25,75,76] The most notable sign for the complexion in the APT data are the peaks in the Li distribution at the crystalline to amorphous transitions at either side of the amorphous interphase. Both experiment and simulation consistently indicate an Al-enrichment in the grain boundary accompanied by an even more pronounced Ti-depletion in the complexion than in the amorphous part.

Apart from demonstrating a generic approach for the atomic-scale characterization of complex buried grain boundaries in modern energy materials, our work provides important leads to the hitherto surprising dendrite suppression capability of LATP inside ASSBs.[37,38] While bulk measurements reveal an electronic conductivity exceeding a recently postulated threshold value for dendrite-free operation,[33] the Ti depletion in the complexion and concomitant increase in Ti–Ti distances across the complexion constitute a sizable barrier for electron transport by polaron hopping. The crystalline grains, which contribute the majority to the bulk Li ion conductivity, are thus encapsulated by an electronically insulating layer. This protects them from reductive decomposition when in contact with Li metal anodes.

Generally, the insights gained in this work highlight that macroscopic bulk measures of ionic and electronic conduction in solid electrolytes alone may not suffice to rationalize processes involved in the deterioration of SSEs by redox decomposition or dendrite nucleation. Such processes depend crucially on the charge carrier dynamics of ions and polarons, and their control correspondingly requires a detailed understanding of local atomistic structure at a level that can presently only be reached by a joint experiment and simulation approach as developed here. Extremely low residual electronic conductivities combined with high ionic mobility might be impossible to achieve as bulk material properties, while sufficient local separation of charge carriers at the nano-scale might suffice and yield sufficient kinetic stabilization of otherwise thermodynamically redox unstable bulk phases at the same time. We will need to extend current ab initio (thermodynamic) approaches and mechanistic studies of polaron and ion migration to include nano-sized motifs like complexions based on realistic atomistically defined structural models to be able to truly design functional buried interfaces in the future.

4. Experimental Section

LATP Sample Preparation: LATP solid electrolyte pellets were prepared as described in an earlier publication by Yu et al.[32] A Li-Al-Ti-P-O powder precursor was first precalcined at 850 °C. Pellets were formed by first uniaxial die pressing at 177 MPa and subsequent cold isostatic pressing at 504 MPa. Sintering was performed at a low heating rate of 0.2 K min^{-1} to a temperature of 1100 °C. This temperature was maintained for 8 h in air atmosphere to obtain a relative density of the LATP pellets of 94.2%. To remove the sintering skin and decrease the electrolyte resistance, the thickness was controlled not to exceed 300 µm by polishing with sand paper (P800).

DC Polarization Measurements: DC polarization measurements were conducted on an LATP pellet of 0.284 mm thickness and 9.82 mm diameter in a Cu/LATP/Cu setup. To improve interfacial connection, the pellet was sputtered with a thin Au layer of ≈300 nm on each side and arranged between two copper ion blocking electrodes. A constant voltage of 11 mV at 50 °C was applied over a polarization time of ≈26 000 s. The DC polarization data is shown in Figure S1, Supporting Information.

TEM Measurements: Samples for HR-TEM were prepared using focused ion beam (FEI, Helios Nanolab 460F1)[77] and measurements were conducted on a FEI Tecnai F20 Microscope[78] operating at 200 kV in TEM mode. STEM images were obtained using HAADF at 80 kV, CA 70 µm, spot 6 in a Titan G2 80-200 CREWLEY[79] microscope with horizontal field width of 34.17 nm. EDS-STEM maps were acquired for about 20 min after a dwell time of 10 µs and a horizontal field width of 44.35 nm. A detailed description of TEM specifications is given in Table S1, Supporting Information. The STEM-HAADF image and the STEM-EDS maps are shown in Figures S2 and S3, Supporting Information.

APT Measurements: APT specimen were prepared by target lift-out method of a polished LATP sample. A dual-beam focused ion beam FEI Helios Nanolab 600i (Thermofisher Scientific, Inc.) with a 30 keV Ga^+ beam was employed for all lift-out and sharpening steps. Final cleaning was performed with a 2 keV Ga^+ beam to remove excess material and reduce Ga contamination. APT analyses were conducted on a reflectron-equipped local electrode atom probe (LEAP 4000X HR, Cameca Instruments) in pulsed laser mode. The laser pulses were tuned to 355 nm wavelength, 12 ps pulse length, 50 pJ pulse energy, and 200 kHz frequency. The detection rate was set to 0.005 ions per pulse at a base temperature of 50 K. The software package IVAS 3.6.14 (Cameca Instruments, Madison, USA) was used for data reconstruction and analysis. APT mass spectra and respective peak assignments are shown in Figure S6, Supporting Information.

Force Field Parameterization: A classical core–shell force field was parameterized for LATP by means of energy matching and force error minimization using the General Utility Lattice Program.[80] DFT reference calculations were obtained using the FHI-aims DFT code[81] and the PBE[82] exchange-correlation functional. Consistent *k*-point grids and scf-convergence criteria were applied. The final parameter set is listed in Table S2, Supporting Information. A detailed description of the parameterization strategy along with extensive force field validation and testing is given in Section S4.1, Supporting Information.

Molecular Dynamics Simulations: Molecular dynamics simulations were performed using the LAMMPS software package.[83] Interatomic interactions were analytically expressed using a Buckingham potential. The polarizable nature of oxygen anions was captured by a core–shell formulation implemented in LAMMPS. A cutoff of 9 Å was chosen for short-range interactions and 3D periodic boundary conditions were applied. Long-range Coulombic interactions were treated by a particle—particle particle-mesh solver.[84] A small timestep of 0.2 fs was chosen for all MD simulations to capture high frequency core–shell vibrations.

TEM Simulations: The DrProbe[51] software package was used to simulate TEM images, where simulation parameters were adopted from TEM experiment if possible. A detector specific modulation transfer function, obtained from the knife edge method,[85] was applied. Simulation parameters are listed in Table S4, Supporting Information. A Scherzer-focus of 63.3 nm, corresponding to the experimentally reported 200 keV laser beam, was chosen. A detailed discussion of the TEM simulation is given in Section S4.3, Supporting Information.

DFT Simulations: Ensemble-DFT calculations for excess charge localization were performed utilizing the pseudo-potential plane wavecode CASTEP.[86] Ultrasoft pseudo potentials provided in the GBRV library[87] were used to describe the atomic core region. A cut-off energy of 750 eV and a *k*-point spacing of 0.07 Å were chosen after convergence testing. Exchange-correlation effects were approximated using the default GGA-level PBE functional.[82]

Supporting Information

Supporting Information is available from the Wiley Online Library or from the author.

Acknowledgements

S.S. acknowledges funding and support from the Deutsche Forschungsgemeinschaft (DFG, German Research Foundation) under Germany's Excellence Strategy - EXC 2089/1- 390776260; and the BMBF (Bundesministerium für Bildung und Forschung) Project EvaBatt (FKZ 03XP0134D). The authors S.S., S.P.R., S.R., S.W., K. R., and C.S. gratefully acknowledge the Leibniz Supercomputing Centre for supporting this project by providing computing time on its Linux-Cluster. R.S. and H.K. acknowledge funding and support from BMBF projects CatSE (FZK 13XP0223A) and LiSI (FZK 13XP0224B).

Open access funding enabled and organized by Projekt DEAL.

Conflict of Interest

The authors declare no conflict of interest.

Data Availability Statement

The data that supports the findings of this study are available in the supplementary material of this article.

Keywords

atom probe tomography, dendrites, density functional theory, molecular dynamics, transmission electron microscopy

Received: March 1, 2021
Revised: April 29, 2021
Published online:

[1] K. Takada, *Acta Mater.* **2013**, *61*, 759.
[2] J. Janek, W. G. Zeier, *Nat. Energy* **2016**, *1*, 16141.
[3] Y. Lu, Z. Tu, L. A. Archer, *Nat. Mater.* **2014**, *13*, 961.
[4] X. Han, Y. Gong, K. Fu, X. He, G. T. Hitz, J. Dai, A. Pearse, B. Liu, H. Wang, G. Rubloff, Y. Mo, V. Thangadurai, E. D. Wachsman, L. Hu, *Nat. Mater.* **2017**, *16*, 572.
[5] J. C. Bachman, S. Muy, A. Grimaud, H. H. Chang, N. Pour, S. F. Lux, O. Paschos, F. Maglia, S. Lupart, P. Lamp, L. Giordano, Y. Shao-Horn, *Chem. Rev.* **2016**, *116*, 140.
[6] L. Wang, J. Li, G. Lu, W. Li, Q. Tao, C. Shi, H. Jin, G. Chen, S. Wang, *Front. Mater.* **2020**, *7*, 111.
[7] A. C. Luntz, J. Voss, K. Reuter, *J. Phys. Chem. Lett.* **2015**, *6*, 4599.
[8] Y. Xiao, Y. Wang, S. H. Bo, J. C. Kim, L. J. Miara, G. Ceder, *Nat. Rev. Mater.* **2020**, *5*, 105.
[9] Z. Zhang, Y. Shao, B. Lotsch, Y. S. Hu, H. Li, J. Janek, L. F. Nazar, C. W. Nan, J. Maier, M. Armand, L. Chen, *Energy Environ. Sci.* **2018**, *11*, 1945.
[10] Y. Zhu, X. He, Y. Mo, *J. Mater. Chem. A* **2016**, *4*, 3253.
[11] C. Chen, M. Jiang, T. Zhou, L. Raijmakers, E. Vezhlev, B. Wu, T. U. Schülli, D. L. Danilov, Y. Wei, R.-A. Eichel, P. H. L. Notten, *Adv. Energy Mater.* **2021**, *11*, 2003939.
[12] T. Yang, Z. D. Gordon, Y. Li, C. K. Chan, *J. Phys. Chem. C* **2015**, *119*, 14947.
[13] E. Glynos, C. Pantazidis, G. Sakellariou, *ACS Omega* **2020**, *5*, 2531.
[14] V. A. Nguyen, C. Kuss, *J. Electrochem. Soc.* **2020**, *167*, 065501.
[15] H. Chen, M. Ling, L. Hencz, H. Y. Ling, G. Li, Z. Lin, G. Liu, S. Zhang, *Chem. Rev.* **2018**, *118*, 8936.
[16] S. Jung, D. W. Kim, S. D. Lee, M. Cheong, D. Q. Nguyen, B. W. Cho, H. S. Kim, *Bull. Korean Chem. Soc.* **2009**, *30*, 2355.
[17] M. Liu, Z. Cheng, S. Ganapathy, C. Wang, L. A. Haverkate, M. Tułodziecki, S. Unnikrishnan, M. Wagemaker, *ACS Energy Lett.* **2019**, *4*, 2336.
[18] R. Koerver, W. Zhang, L. De Biasi, S. Schweidler, A. O. Kondrakov, S. Kolling, T. Brezesinski, P. Hartmann, W. G. Zeier, J. Janek, *Energy Environ. Sci.* **2018**, *11*, 2142.
[19] Y. Zhu, X. He, Y. Mo, *ACS Appl. Mater. Interfaces* **2015**, *7*, 23685.
[20] D. Cao, X. Sun, Q. Li, A. Natan, P. Xiang, H. Zhu, *Matter* **2020**, *3*, 57.
[21] W. D. Richards, L. J. Miara, Y. Wang, J. C. Kim, G. Ceder, *Chem. Mater.* **2016**, *28*, 266.
[22] P. Albertus, S. Babinec, S. Litzelman, A. Newman, *Nat. Energy* **2018**, *3*, 16.
[23] A. Urban, D. H. Seo, G. Ceder, *npj Comput. Mater.* **2016**, *2*, 16002.
[24] J. Luo, *J. Mater.* **2015**, *1*, 22.
[25] J. Luo, *Energy Storage Mater.* **2019**, *21*, 50.
[26] P. R. Cantwell, T. Frolov, T. J. Rupert, A. R. Krause, C. J. Marvel, G. S. Rohrer, J. M. Rickman, M. P. Harmer, *Annu. Rev. Mater. Res.* **2020**, *50*, 465.
[27] S. J. Dillon, M. P. Harmer, *J. Eur. Ceram. Soc.* **2008**, *28*, 1485.
[28] B. Wu, S. Wang, J. Lochala, D. Desrochers, B. Liu, W. Zhang, J. Yang, J. Xiao, *Energy Environ. Sci.* **2018**, *11*, 1803.
[29] L. Li, Z. Zhang, L. Luo, J. Jiao, W. Huang, J. Wang, C. Li, X. Han, S. Chen, *Ionics (Kiel)* **2020**, *26*, 3815.
[30] M. Kick, C. Scheurer, H. Oberhofer, *J. Chem. Phys.* **2020**, *153*, 14.
[31] M. Kick, C. Grosu, M. Schuderer, C. Scheurer, H. Oberhofer, *J. Phys. Chem. Lett.* **2020**, *11*, 2535.
[32] S. Yu, D. J. Siegel, *ACS Appl. Mater. Interfaces* **2018**, *10*, 38151.
[33] F. Han, A. S. Westover, J. Yue, X. Fan, F. Wang, M. Chi, D. N. Leonard, N. J. Dudney, H. Wang, C. Wang, *Nat. Energy* **2019**, *4*, 187.
[34] H. Aono, E. Sugimoto, Y. Sadaoka, N. Imanaka, G. ya Adachi, *Solid State Ionics* **1990**, *40–41*, 38.
[35] H. Aono, E. Sugimoto, Y. Sadaoka, N. Imanaka, G.-y. Adachi, *J. Electrochem. Soc.* **1990**, *137*, 1023.
[36] G. J. Redhammer, D. Rettenwander, S. Pristat, E. Dashjav, C. M. Kumar, D. Topa, F. Tietz, *Solid State Sci.* **2016**, *60*, 99.
[37] S. Yu, A. Mertens, H. Tempel, R. Schierholz, H. Kungl, R. A. Eichel, *ACS Appl. Mater. Interfaces* **2018**, *10*, 22264.
[38] S. Yu, S. Schmohl, Z. Liu, M. Hoffmeyer, N. Schön, F. Hausen, H. Tempel, H. Kungl, H. D. Wiemhöfer, R. A. Eichel, *J. Mater. Chem. A* **2019**, *7*, 3882.
[39] S. Kasap, P. Capper, *Springer Handbook of Electronic and Photonic Materials*, Springer, Cham **2017**.
[40] J. Maier, *Nat. Mater.* **2010**, *4*, 160.
[41] J. Maier, *Chem. Mater.* **2014**, *26*, 348.
[42] A. M. Nolan, Y. Zhu, X. He, Q. Bai, Y. Mo, *Joule* **2018**, *2*, 2016.
[43] S. Shi, J. Gao, Y. Liu, Y. Zhao, Q. Wu, W. Ju, C. Ouyang, R. Xiao, *Chinese Phys. B* **2016**, *25*, 018212.
[44] Y. Sun, T. Yang, H. Ji, J. Zhou, Z. Wang, T. Qian, C. Yan, *Adv. Energy Mater.* **2020**, *10*, 2002373.
[45] R. Jalem, K. Kanamori, I. Takeuchi, M. Nakayama, H. Yamasaki, T. Saito, *Sci. Rep.* **2018**, *8*, 5845.
[46] H. H. Heenen, J. Voss, C. Scheurer, K. Reuter, A. C. Luntz, *J. Phys. Chem. Lett.* **2019**, *10*, 2264.
[47] J. S. Kim, W. D. Jung, J. W. Son, J. H. Lee, B. K. Kim, K. Y. Chung, H. G. Jung, H. Kim, *ACS Appl. Mater. Interfaces* **2019**, *11*, 13.
[48] T. Hupfer, *Herstellung von LATP für den Einsatz als Festkörperelektrolyt und dessen Eigenschaften*, KIT Scientific Publishing, Karlsruhe **2017**.
[49] S. Yu, A. Mertens, X. Gao, D. C. Gunduz, R. Schierholz, S. Benning, F. Hausen, J. Mertens, H. Kungl, H. Tempel, R. A. Eichel, *Funct. Mater. Lett.* **2016**, *9*, 1650066.
[50] D. C. Gunduz, R. Schierholz, S. Yu, H. Tempel, H. Kungl, R. A. Eichel, *J. Adv. Ceram.* **2020**, *9*, 149.

[51] J. Barthel, *Ultramicroscopy* **2018**, *193*, 1.
[52] A. Mertens, S. Yu, N. Schön, D. C. Gunduz, H. Tempel, R. Schierholz, F. Hausen, H. Kungl, J. Granwehr, R. A. Eichel, *Solid State Ionics* **2017**, *309*, 180.
[53] Y. Yoon, J. Kim, C. Park, D. Shin, *J. Ceram. Process. Res.* **2013**, *14*, 563.
[54] A. S. Best, M. Forsyth, D. R. MacFarlane, *Solid State Ionics* **2000**, *136–137*, 339.
[55] S. Choi, B. N. Yun, W. D. Jung, T. H. Kim, K. Y. Chung, J. W. Son, B. I. Sang, H. G. Jung, H. Kim, *Scr. Mater.* **2019**, *165*, 10.
[56] A. Devaraj, M. Gu, R. Colby, P. Yan, C. M. Wang, J. M. Zheng, J. Xiao, A. Genc, J. G. Zhang, I. Belharouak, D. Wang, K. Amine, S. Thevuthasan, *Nat. Commun.* **2015**, *6*, 8014.
[57] A. Devaraj, C. Szymanski, P. Yan, C. Wang, V. Murgesan, J. M. Zheng, J. Zhang, T. Tyliszczak, S. Thevuthasan, *Microsc. Microanal.* **2015**, *21*, 685.
[58] A. Devaraj, R. Colby, W. P. Hess, D. E. Perea, S. Thevuthasan, *J. Phys. Chem. Lett.* **2013**, *4*, 993.
[59] J. Maier, B. Pfeiffer, C. A. Volkert, C. Nowak, *Energy Technol.* **2016**, *4*, 1565.
[60] P. Hartman, H. K. Chan, *Pharm. Res.* **1993**, *10*, 1052.
[61] Y. Liang, H. Dong, D. Aurbach, Y. Yao, *Nat. Energy* **2020**, *5*, 646.
[62] M. Li, J. Lu, X. Ji, Y. Li, Y. Shao, Z. Chen, C. Zhong, K. Amine, *Nat. Rev. Mater.* **2020**, *5*, 276.
[63] J. Yang, G. Liu, M. Avdeev, H. Wan, F. Han, L. Shen, Z. Zou, S. Shi, Y. S. Hu, C. Wang, X. Yao, *ACS Energy Lett.* **2020**, *5*, 2835.
[64] P. Hu, Z. Zou, X. Sun, D. Wang, J. Ma, Q. Kong, D. Xiao, L. Gu, X. Zhou, J. Zhao, S. Dong, B. He, M. Avdeev, S. Shi, G. Cui, L. Chen, *Adv. Mater.* **2020**, *32*, 1907526.
[65] L. Priester, *Grain Boundaries*, Springer Series in Materials Science, Springer, Dordrecht, **2013**, pp. 49–92.
[66] S. Yu, D. J. Siegel, *Chem. Mater.* **2017**, *29*, 9639.
[67] J. A. Dawson, P. Canepa, T. Famprikis, C. Masquelier, M. S. Islam, *J. Am. Chem. Soc.* **2018**, *140*, 362.
[68] K. Shen, Y. Wang, J. Zhang, Y. Zong, G. Li, C. Zhao, H. Chen, *Phys. Chem. Chem. Phys.* **2020**, *22*, 3030.
[69] G. Bergerhoff, I. D. Brown, in *Crystallographic Databases* (Ed: F. H. Allen), Chester, International Union of Crystallography **1987**, https://icsd.products.fiz-karlsruhe.de/en/about/about-icsd#publications.
[70] M. Monchak, O. Dolotko, M. J. Mühlbauer, V. Baran, A. Senyshyn, H. Ehrenberg, *Solid State Sci.* **2016**, *61*, 161.
[71] D. Pfalzgraf, D. Mutter, D. F. Urban, *Solid State Ionics* **2021**, *359*, 115521.
[72] J. L. Narváez-Semanate, A. C. Rodrigues, *Solid State Ionics* **2010**, *181*, 1197.
[73] A. J. Cohen, P. Mori-Sánchez, W. Yang, *Science (80-.)* **2008**, *321*, 792.
[74] H. Oberhofer, K. Reuter, J. Blumberger, *Chem. Rev.* **2017**, *117*, 10319.
[75] W. D. Kaplan, D. Chatain, P. Wynblatt, W. C. Carter, *J. Mater. Sci.* **2013**, *48*, 5681.
[76] P. R. Cantwell, M. Tang, S. J. Dillon, J. Luo, G. S. Rohrer, M. P. Harmer, *Acta Mater.* **2014**, *62*, 1.
[77] M. Kruth, D. Meertens, K. Tillmann, *J. Large-Scale Res. Facil.* **2016**, *2*, A59.
[78] M. Luysberg, M. Heggen, K. Tillmann, *J. Large-Scale Res. Facil.* **2016**, *2*, A77.
[79] A. Kovács, R. Schierholz, K. Tillmann, *J. Large-Scale Res. Facil.* **2016**, *2*, 68.
[80] J. D. Gale, A. L. Rohl, *Mol. Simul.* **2003**, *29*, 291.
[81] V. Blum, R. Gehrke, F. Hanke, P. Havu, V. Havu, X. Ren, K. Reuter, M. Scheffler, *Comput. Phys. Commun.* **2009**, *180*, 2175.
[82] J. P. Perdew, K. Burke, M. Ernzerhof, *Phys. Rev. Lett.* **1996**, *77*, 3865.
[83] S. Plimpton, *J. Comput. Phys.* **1995**, *117*, 1.
[84] R. W. Hockney, J. W. Eastwood, *Computer Simulation Using Particles*, CRC Press, Boca Raton, FL **1988**.
[85] A. Thust, *Phys. Rev. Lett.* **2009**, *102*, 5.
[86] S. J. Clark, M. D. Segall, C. J. Pickard, P. J. Hasnip, M. I. Probert, K. Refson, M. C. Payne, *Z. Kristallogr.* **2005**, *220*, 567.
[87] K. F. Garrity, J. W. Bennett, K. M. Rabe, D. Vanderbilt, *Comput. Mater. Sci.* **2014**, *81*, 446.